MOX-Report No. 01/2024

Computational haemodynamics for pulmonary valve replacement by means of a reduced Fluid-Structure Interaction model

Criseo, M.; Fumagalli, I.; Quarteroni, A.; Marianeschi, S. M.; Vergara, C.

MOX, Dipartimento di Matematica
Politecnico di Milano, Via Bonardi 9 - 20133 Milano (Italy)

mox-dmat@polimi.it https://mox.polimi.it

Computational haemodynamics for pulmonary valve replacement by means of a reduced Fluid-Structure Interaction model

Elisabetta Criseo[1,2], Ivan Fumagalli[3], Alfio Quarteroni[3,4], Stefano Maria Marianeschi[5], Christian Vergara[1]

[1] LaBS, Dipartimento di Chimica, Materiali e Ingegneria Chimica, Politecnico di Milano, Milan, Italy
[2] Centro Cardiologico Monzino IRCCS, Milan, Italy
[3] MOX, Dipartimento di Matematica, Politecnico di Milano, Milan, Italy
[4] Institute of Mathematics, École Polytechnique Fédérale de Lausanne, Lausanne, Switzerland
[5] Cardiac Surgery, ASST Grande Ospedale Metropolitano Niguarda, Milan, Italy

Abstract

Pulmonary Valve Replacement (PVR) consists of substituting a patient's original valve with a prosthetic one, primarily addressing pulmonary valve insufficiency, which is crucially relevant in Tetralogy of Fallot repairment. While extensive clinical and computational literature on aortic and mitral valve replacements is available, PVR's post-procedural haemodynamics in the pulmonary artery and the impact of prosthetic valve dynamics remain significantly understudied.

Addressing this gap, we introduce a reduced Fluid-Structure Interaction (rFSI) model, applied for the first time to the pulmonary valve. This model couples a three-dimensional computational representation of pulmonary artery haemodynamics with a one-degree-of-freedom model to account for valve structural mechanics. Through this approach, we analyse patient-specific haemodynamics pre and post PVR. Patient-specific geometries, reconstructed from CT scans, are virtually equipped with a template valve geometry. Boundary conditions for the model are established using a lumped-parameter model, fine-tuned based on clinical patient data.

Our model accurately reproduces patient-specific haemodynamic changes across different scenarios: pre-PVR, six months post-PVR, and a follow-up condition after a decade. It effectively demonstrates the impact of valve implantation on sustaining the diastolic pressure gradient across the valve. Preliminary outcomes indicate the reliability of our valve model concerning the robustness of its application across various patients, despite being calibrated initially with data from a single patient. This promising approach provides insights into post-PVR haemodynamics and prosthetic valve effects, shedding light on potential implications for patient-specific outcomes.

Keywords – Pulmonary valve replacement, Tetralogy of Fallot, image-based computational fluid dynamics, reduced fluid-structure interaction, patient-specific analysis

1 Introduction

Valve replacement is a surgical treatment extensively used on patients with advanced valvular heart disease; it consists in the replacement of the patient's native valve with a prosthetic one [1, 2]. In the clinical literature, the most studied procedures are aortic and mitral valve replacement [3, 4, 5, 6, 7], however, valve replacement is an option also in the case of Pulmonary Valve (PV) pathologies and research about this procedure is increasing. The necessity for Pulmonary Valve Replacement (PVR) is mainly linked to Congenital Heart Diseases (CHDs) that can present valvular malformations or involve the complete absence of a valve.

One of the most studied CHDs leading to PVR is the *Tetralogy Of Fallot* (TOF), which has an incidence of 3 to 5 every 10,000 newborns and accounts for 7% to 10% of all congenital malformations [8]. This pathology consists in a tetrad of heart defects involving the ventricles, the ventricular septum, the Right Ventricle Outflow Tract (RVOT) and the aorta. The repair of the defects, especially the intervention on the RVOT, impacts also on pulmonary valve morphology, thus often yielding pulmonary regurgitation [9, 10, 11]. This eventually translates to the necessity of a subsequent PVR, as indicated by clinical guidelines [12]. Indeed, although pulmonary regurgitation is often well tolerated by patients, a long-term effect of this condition can be an increase in the volume load to the right ventricle

and consequently its dilation, which then increases the risk of arrhythmias [9]. Another example of a surgical procedure leading to the need for a PVR is the *Ross procedure*, that is the substitution of the aortic valve with a pulmonary valve autograft, performed in the presence of an anomaly in the aortic valve morphology or function [13]. Consequently, the patient is left with a valveless conduit at the RVOT, leading to pulmonary insufficiency. Again, this condition must be treated with PVR to avoid an increased risk of arrhythmia and heart failure.

Mathematical and numerical models have been increasingly used to study pathologies and support clinical research, providing quantitative analyses of the mechanisms characterising the cardiovascular system. Pulmonary circulation can be mathematically modelled using different approaches. Lumped parameters models, describe, through a system of ordinary differential equations, the time evolution of flow rate and pressure mean values over compartments that represent the cardiovascular system [14, 15, 16]. This allows having a simplified model which provides analytical measures of the principal haemodynamics quantities. In a clinical framework, this approach can be extremely resourceful since it is not computationally demanding and can be used to replicate the effect on the haemodynamics of different therapeutic approaches [17, 18, 19]. Another tool used to model the cardiovascular system are three-dimensional models, which describe the haemodynamics with a higher degree of detail with respect to lumped parameters models. Standalone 3D models of the pulmonary artery have been extensively used within the framework of Computational Fluid Dynamics (CFD) to analyse how haemodynamics vary with respect to physiological [20] and pathological settings, such as pulmonary hypertension [21] and congenital heart diseases [22], but also as a consequence of surgical procedures [23, 24]. However, these models are not able to describe the interactions between local haemodynamics and systemic circulation. To this aim, lumped parameters models can be used to provide boundary conditions to a 3D domain, such as the pulmonary artery[25], with the objective, for example, of verifying the haemodynamic effect of different surgical procedures for the repairment of congenital heart diseases [26, 27].

The mathematical models described above could be further improved by taking into account the interaction between the fluid and the surrounding structures, namely adopting a Fluid-Structure Interaction (FSI) approach. The interaction of the fluid with the arterial wall has been studied in a healthy setting [28, 29] but also in the pathological framework of pulmonary arterial hypertension [30, 31]; however, to our knowledge, there is a lack of studies reporting the FSI modelling of the pulmonary valve.

This study has two main objectives:

1. The development and calibration of a *reduced FSI model*, consisting on the coupling between a 3D model of the pulmonary artery and a *one-degree-of-freedom* mechanical model for the valve.
2. The application of the developed model to the clinical case of two patients who underwent the replacement of the pulmonary valve. For each of them, we modelled three scenarios to compare pre-implantation, post-implantation, and follow-up conditions.

The main novelty of this study is the use of the reduced FSI model, which allows the reproduction of haemodynamics influenced by the presence of the valve that moves immersed in the fluid. To our knowledge, this is the first time that this kind of model has been applied to the study of pulmonary valve replacement. Moreover, being the study patient-specific, it allows to assess the applicability of the model to clinical conditions.

The paper has the following outline. In Section 2, we describe the mathematical methods and numerical models used. In Section 3.1 we discuss the clinical scenarios and the calibration of the models, whereas in Section 3.2 the geometry reconstruction and mesh generation processes are detailed. Finally, in Section 4 we present the results of the model application on the patients' case and we discuss the significance of the findings.

2 Models and methods

In this section, we want to outline the reduced Fluid-Structure Interaction (rFSI) model used in this study, which is based on the coupling between a 3D pulmonary artery model and a reduced pulmonary valve model where the opening is described by a single degree of freedom. We start by describing the continuous problems, consisting in the 3D blood flow dynamics, the one-degree-of-freedom valve mechanical model, and their coupling (Section 2.1). Then, we proceed by defining the corresponding numerical approximations in time and space (Section 2.2). Finally, we discuss the boundary conditions for the 3D problem, provided by a lumped parameter model of the cardiocirculatory system (Section 2.3).

2.1 Reduced Fluid-Structure Interaction model

This mathematical model aims to describe the haemodynamics in the pulmonary artery, from the Right Ventricle Outflow Tract (RVOT), where the pulmonary valve is located, to its two main bifurcations.

The choice of a rigid wall model for blood fluid dynamics, defined by using Navier-Stokes equations, is a consequence of the decision to neglect the artery wall compliance since the pulmonary artery is characterised by low pressure and

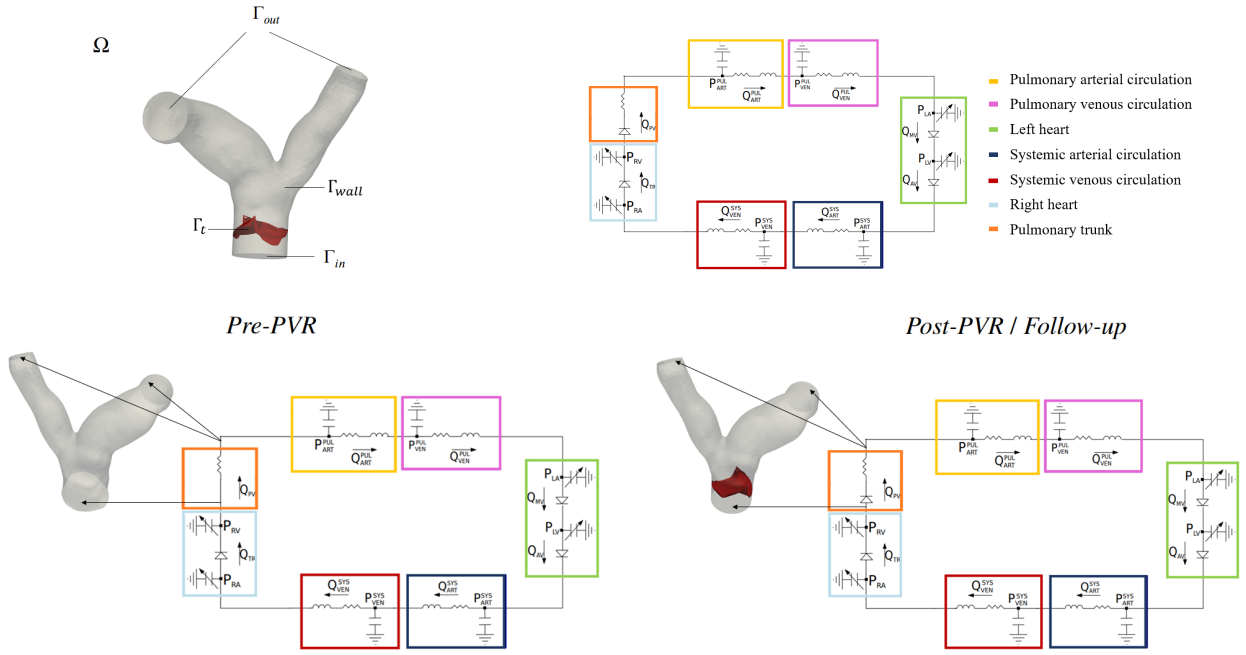

Figure 1: Top-left: schematic representation of the domain Ω, of the physical and artificial boundaries $\Gamma_{wall}, \Gamma_{in}, \Gamma_{out}$, and of the pulmonary valve surface Γ_t; Top-right: Schematic representation of the Lumped Parameters Model of the whole circulation; Bottom: Lumped Parameters Models used for the *Pre-PVR* scenario (left) and for the *Post-PVR* and *Follow-up* scenarios (right).

small deformations. This is a widely accepted hypothesis, despite a slight overestimation of the Wall Shear Stress (WSS) is introduced [32]. Furthermore, as commonly accepted, the blood is modelled as a homogeneous, Newtonian and incompressible fluid, due to its composition and due to the fact that we are analysing haemodynamics in a large vessel, namely the pulmonary artery [33, 34].

Referring to Fig. 1, top-left, we denote the fixed pulmonary artery domain by Ω, the artery wall by Γ_{wall}, the inlet/outlet sections by Γ_{in}/Γ_{out}, and the moving immersed valve surface by Γ_t. In this domain, the strong formulation of the problem reads:
Given the initial blood velocity $\mathbf{u}(t, \mathbf{x}) = \mathbf{0}$ at $t = 0$, for each time $t > 0$, find the blood velocity $\mathbf{u}$ and the blood pressure p, such that:

$$\begin{cases} \rho \dfrac{\partial \mathbf{u}}{\partial t} + \rho(\mathbf{u} \cdot \nabla)\mathbf{u} - \nabla \cdot \mathbf{T}_F + \dfrac{R}{\varepsilon}(\mathbf{u} - \alpha \mathbf{u}_\Gamma)\delta_{\Gamma_t,\varepsilon} = \mathbf{0} & in\ \Omega, \\ \nabla \cdot \mathbf{u} = 0 & in\ \Omega, \end{cases} \tag{1}$$

with $\mathbf{T}_F(\mathbf{u}, p) = -p\mathbf{I} + (\mu + \mu_{sgs})(\nabla \mathbf{u} + \nabla \mathbf{u}^T)$ the Cauchy stress tensor. The system is completed with no-slip conditions on Γ_{wall} and boundary conditions on Γ_{in} and Γ_{out} coming from a lumped parameter model, see Section 2.3. In the Cauchy stress tensor, the presence of the sub-grid viscosity $\mu_{sgs} = \mu_{sgs}(\mathbf{u})$ is related to the adoption of the Large Eddy Simulation (LES) σ-model, successfully used to capture transitions to turbulence in haemodynamics [35, 36, 37].

Notice that the presence of the valve is considered by adopting the Resistive Immersed Implicit Surface (RIIS) method [38, 39, 40], which implies the addition of a resistive penalty term $\frac{R}{\varepsilon}(\mathbf{u} - \alpha \mathbf{u}_\Gamma)\delta_{\Gamma_t,\varepsilon}$ to the momentum conservation equation. This includes the ratio between a resistance R, which acts as the penalty parameter, and the thickness ε of the leaflets. We remark that the resistive term has support only in a narrow layer around Γ_t, representing the moving valve leaflets surface; in the equation, this is described by the smoothed Dirac delta $\delta_{\Gamma_t,\varepsilon}$. This term has the aim of enforcing the blood velocity $\mathbf{u}$ to be equal to a given field $\alpha \mathbf{u}_\Gamma$ in proximity of the leaflets surface, $\alpha \in [0, 1]$ being a parameter to be properly selected to enhance stability.

A mechanical model of the valve, suitably coupled with the blood dynamics problem (1), is required to obtain the current valve configuration Γ_t and the valve surface velocity $\mathbf{u}_\Gamma$. The one-degree-of-freedom (1-DoF) mechanical model introduced in [41] is chosen in order to reduce the computational effort demanded by the solution of a whole 3D FSI model, while still taking into account the presence of the valve and its encumbrance in the RVOT. Specifically, we describe the valve configuration by a single unknown variable $c = c(t)$, representing the opening fraction of the valve

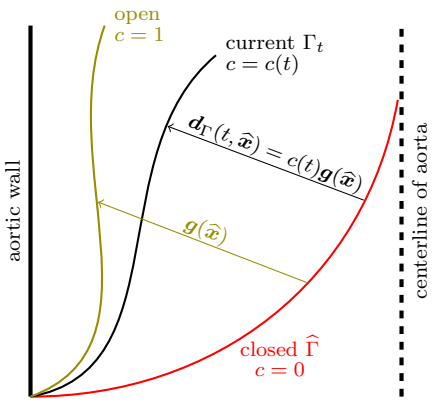

Figure 2: Schematic representation of the 1-DoF model for the valve. The current position Γ_t of the valve (black) is determined from its fully closed (red) and fully open (green) configuration, in terms of the opening coefficient $c(t)$, see (2).

itself. As represented in Fig. 2, the current valve configuration Γ_t is then defined in terms of the following function:

$$\mathbf{d}_\Gamma(t, \widehat{\mathbf{x}}) = c(t)\mathbf{g}(\widehat{\mathbf{x}}), \tag{2}$$

where, here and in what follows, quantities with the $\widehat{\cdot}$ refer to the reference configuration, $\mathbf{d}_\Gamma : [0, T] \times \widehat{\Gamma} \to \mathbb{R}^3$ denotes the displacement of the leaflet and $\mathbf{g} : \widehat{\Gamma} \to \mathbb{R}^3$ is the displacement between the fully closed and fully open configurations, which are known from imaging, see Section 3.2. Thus, the 1-DoF structure model in the unknown c reads as follows [41]:

$$\ddot{c} = -\beta\dot{c} + \frac{\int_{\Gamma_t} \mathbf{f}(t, \mathbf{x}) \cdot \mathbf{n}_\Gamma(\mathbf{x})\, d\mathbf{x} - \gamma \int_{\Gamma_t} [H(\mathbf{x}) - \widehat{H}(\widehat{\mathbf{x}}) - \chi]\, d\mathbf{x}}{\int_{\Gamma_t} \rho_\Gamma \mathbf{g}(\widehat{\mathbf{x}}) \cdot \mathbf{n}_\Gamma(\mathbf{x})\, d\mathbf{x}}, \tag{3}$$

where H is the leaflets curvature, $\mathbf{n}_\Gamma$ is the normal to Γ_t, β is the damping coefficient, γ is the stiffness, ρ_Γ is the surface density, and χ is a suitable coefficient ensuring that the curvature term is responsible for the valve closure. This ordinary differential equation is completed by suitable initial conditions on $c(0)$ and $\dot{c}(0)$. In this study, we assume that the valve is initially closed and still: $c(0) = 0$ and $\dot{c}(0) = 0$.

To couple the 3D fluid model (1) and the 1-DoF valve model (3) we need the kinematic and dynamic coupling conditions. The kinematic condition is represented by the resistive penalty term $\frac{R}{\varepsilon}(\mathbf{u} - \alpha\mathbf{u}_\Gamma)\delta_{\Gamma_t,\varepsilon}$ in (1), with $\mathbf{u}_\Gamma = \dot{\mathbf{d}}_\Gamma = \dot{c}\mathbf{g}$. The dynamic condition is given by the force balance $\mathbf{f} = \mathbf{T}_F\mathbf{n}_\Gamma$ on Γ_t. Here and in (3), greek letters indicate parameters that need to be suitably calibrated, see Section 3.3.2.

This coupling leads to the following reduced[1] FSI (rFSI) problem:
Given the valve displacement $\mathbf{g}$ mapping the fully closed configuration to the fully open one, find $\mathbf{u}, p, c, z$ for each $t \in (0, T]$, such that:

$$\text{structure problem} \begin{cases} \dot{c} = z, \\ \dot{z} = \eta(\Gamma_t, \mathbf{f}, H, c, z; \beta, \gamma, \chi, \rho_\Gamma, \mathbf{g}), \end{cases} \tag{4a}$$

$$\text{coupling} \begin{cases} \Gamma_t = \{\widehat{\mathbf{x}} + c\ \mathbf{g}(\widehat{\mathbf{x}}) : \widehat{\mathbf{x}} \in \widehat{\Gamma}\}, \\ \mathbf{u}_\Gamma = \dot{c}\ \mathbf{g} \quad on\ \Gamma_t, \\ \mathbf{f} = \mathbf{T}_F\mathbf{n}_\Gamma \quad on\ \Gamma_t, \end{cases} \tag{4b}$$

$$\text{fluid problem} \begin{cases} \rho\dfrac{\partial \mathbf{u}}{\partial t} + \rho(\mathbf{u} \cdot \nabla)\mathbf{u} - \nabla \cdot \mathbf{T}_F + \dfrac{R}{\varepsilon}(\mathbf{u} - \alpha\mathbf{u}_\Gamma)\delta_{\Gamma_t,\varepsilon} = 0 & in\ \Omega, \\ \nabla \cdot \mathbf{u} = 0 & in\ \Omega, \end{cases} \tag{4c}$$

where the structure problem is written as a system of first-order ordinary differential equations with $\eta(\Gamma_t, \mathbf{f}, H, c, z; \beta, \gamma, \chi, \rho_\Gamma, \mathbf{g})$ as the right-hand side of (3).

[1]Notice that with "reduced", here we mean that the model is given by using a 1-DoF valve model rather than a 3D one. As a consequence, we stress that we are not considering *reduced order modelling*, nor a lumped parameter diode representation

2.2 Numerical approximation

The rFSI model (4) is discretised both in time and space. We introduce a uniform partition of the time interval $[0, T]$ with step-size Δt; the partition has nodes $\{t^n\}_{n=0}^N$ and the step-size is defined as $\Delta t = T/N$. Considering a generic function $v(t)$, v^n indicates the approximation of $v(t^n)$. Therefore, the time-discretised rFSI problem reads:

$$\text{structure problem} \begin{cases} \begin{bmatrix} c^n \\ z^n \end{bmatrix} = \widetilde{\boldsymbol{\eta}} \left(\Gamma^{n-1}, \mathbf{f}^{n-1}, H^{n-1}, c^{n-1}, z^{n-1}; \beta, \gamma, \chi, \rho_\Gamma, \mathbf{g} \right), \end{cases} \tag{5a}$$

$$\text{kinematic coupling} \begin{cases} \Gamma^n = \{\widehat{\mathbf{x}} + c^n \mathbf{g}(\widehat{\mathbf{x}}) : \widehat{\mathbf{x}} \in \widehat{\Gamma}\}, \\ \mathbf{u}_\Gamma^n = \dfrac{c^n - c^{n-1}}{\Delta t} \mathbf{g} \text{ on } \Gamma^n, \end{cases} \tag{5b}$$

$$\text{fluid problem} \begin{cases} \rho \dfrac{\mathbf{u}^n - \mathbf{u}^{n-1}}{\Delta t} + \rho(\mathbf{u}^{n-1} \cdot \nabla)\mathbf{u}^n - \nabla \cdot \mathbf{T}_F^n + \dfrac{R}{\varepsilon}(\mathbf{u}^n - \alpha \mathbf{u}_\Gamma^n)\delta_\varepsilon^n = 0 \quad in\ \Omega, \\ \nabla \cdot \mathbf{u}^n = 0 \qquad\qquad\qquad\qquad\qquad\qquad\qquad\qquad\qquad\quad in\ \Omega. \end{cases} \tag{5c}$$

$$\text{dynamic coupling} \begin{cases} \mathbf{f}^n = \mathbf{T}_F^n \mathbf{n}_\Gamma^n \quad \text{on } \Gamma^n. \end{cases} \tag{5d}$$

where $\widetilde{\boldsymbol{\eta}}$ is defined by the discretisation of (4a) with the classical fourth-order, explicit Runge-Kutta method [42].

The time discretisation for the 3D fluid model (5c) is carried out by means of the Backwards Differentiation Formula (BDF) of order 1 with a semi-implicit treatment for the non-linear term $\rho(\mathbf{u} \cdot \nabla)\mathbf{u}$ in (1). The space discretisation of the fluid problem is carried out by the Finite Element (FE) method of order 1 for both velocity and pressure with a SUPG-PSPG stabilisation [43, 44]. As for the 1-DoF valve model, the assembly of the right-hand side $\widetilde{\boldsymbol{\eta}}$ hinges upon the RIIS representation of the valve surface Γ^n and normal vector $\mathbf{n}_\Gamma^n$, as discussed in [41].

The fluid and structure models are then weakly (explicitly-in-time) coupled at each time step, meaning that the 3D fluid model and the 1-DoF structure model exchange information only once per time step. Specifically, at each t^n, the structure problem (5a) is solved by using the fluid interface force $\mathbf{f}^{n-1}$ taken from the previous time step, and the new interface position and velocity are computed using the kinematic coupling conditions (5b). Then, the fluid problem (5c) is solved accordingly. This scheme is summarised in Algorithm 1:

Algorithm 1 Scheme for the solution of the rFSI model

Given $\mathbf{u}_h^0, p_h^0, c^0$ and the initial surface Γ^0

1: **for** $n = 1$ to N **do**
2: Compute the fluid force $\mathbf{f}^{n-1}$ and the integrals that make up (3), in terms of $\mathbf{u}_h^{n-1}, p_h^{n-1}, \Gamma^{n-1}$;
3: Find c^n by advancing the 0D equation (5a) with a step of the explicit fourth-order Runge-Kutta method;
4: Create the immersed surface Γ^n moving the previous configuration Γ^{n-1} by $\mathbf{d}_\Gamma^n - \mathbf{d}_\Gamma^{n-1} = (c^n - c^{n-1})\mathbf{g}$;
5: Compute the leaflets velocity $\mathbf{u}_\Gamma^n = \dfrac{c^n - c^{n-1}}{\Delta t} \mathbf{n}_{\Gamma,h}^n$;
6: Find $(\mathbf{u}_h^n, p_h^n)$ by solving the fluid problem (5c).
7: **end for**

Algorithm 1 has been solved in the computational fluid dynamics module `life`$^{\mathtt{x}}$`-cfd` [45] of `life`$^{\mathtt{x}}$ [46, 47], a high-performance library for the finite element simulations of multiphysics, multiscale, and multidomain problems, developed within the iHeart project (`https://iheart.polimi.it/`), at the MOX laboratory of the Department of Mathematics - Politecnico di Milano.

2.3 Boundary conditions: lumped parameters model of the circulation

In order to obtain suitable boundary conditions for the artificial boundaries $\Gamma_{in}, \Gamma_{out}$ of the 3D computational domain, we introduce a closed-loop Lumped Parameters Model (LPM) of the whole circulatory system (Fig. 1, top-right) proposed in [48, 49, 25], which is solved once and for all before the starting of the 3D simulation (*One-Way* coupling).

In this LPM we model the pulmonary valve as a non-ideal diode represented by a variable resistance $R = 10^b$, with b defined as:

$$b = \log_{10} R_{min} \ + \ (\log_{10} R_{max} - \log_{10} R_{min}) \cdot \left[\frac{1}{2} + \frac{1}{\pi} \arctan\left(\frac{k\pi}{2} (P_{\text{ART}}^{\text{PUL}} - P_{\text{RV}}) \right) \right],$$

where R_{max} is the resistance when the valve is closed, R_{min} is the resistance when the valve is open, and $P_{\text{ART}}^{\text{PUL}}$, P_{RV} are the pulmonary artery pressure and right ventricle pressure indicated in Fig. 1, top-right [25].

Since the 3D model corresponds to the 0D pulmonary trunk district (orange in Fig. 1, top-right), a possible choice for the boundary conditions on Γ_{in}, Γ_{out} are the following:

$$\begin{cases} \mathbf{T}_F(\mathbf{u}^n, p^n)\mathbf{n} = P_{RV}(t^n)\mathbf{n} \quad on\ \Gamma_{in}, \\ \mathbf{T}_F(\mathbf{u}^n, p^n)\mathbf{n} = P_{ART}^{PUL}(t^n)\mathbf{n} \quad on\ \Gamma_{out}, \end{cases} \tag{6}$$

where the solution of the LPM was found using the explicit fourth-order Runge-Kutta scheme.

The LPM parameters are suitably tuned in order to adhere as much as possible to the values of the patients' available clinical data (see Section 3.3.1).

The LPM is solved in the library `life`$^{\text{x}}$ [46, 47].

3 Reconstruction procedure and scenarios outline

In order to carry out a patient-specific analysis of pulmonary artery haemodynamics, we rely on the study of two patients' clinical data. The patients, P1 and P2, were left without a pulmonary valve for decades, after having undergone the Ross procedure in the treatment of their Tetralogy of Fallot. Then, they were subject to Pulmonary Valve Replacement (PVR), with the implantation of the *No-React® BioPulmonic™* valve, composed by porcine pulmonary leaflets surrounded by a bovine pericardium sleeve, which are mounted on a self-expandable Nitinol stent [50].

We build the geometric configurations of both before (*pre-implantation* scenario) and after (*post-implantation* scenario) the PVR, together with a *follow-up* scenario after 9 years, to evaluate the impact of the prosthetic valve on haemodynamics. To this aim, in the following of this section we describe the building-up of the three computational scenarios (Section 3.1), the reconstruction of the 3D fluid domain from the patients' CT scans (Section 3.2), and the calibration of the valve parameters in the rFSI model and of the LPM parameters (Section 3.3).

3.1 Computational scenarios

We introduce the three computational scenarios (Fig. 1, bottom) used for each patient:

1. *Pre-PVR*: the pre-implantation scenario is characterised by the absence of the valve. Accordingly, in the rFSI model (5) we set $R = 0$, whereas in the LPM we set $R_{max} = R_{min} = 2.2 \cdot 10^{-2}$ mmHg s ml^{-1}. Notice that in this case the rFSI model is in fact a CFD model, due to the absence of the valve;
2. *Post-PVR*: the prosthetic valve is implanted, so we use the rFSI model (5) with $R = 10^4$ kg m^{-1} s^{-1} and the LPM with $R_{max} >> R_{min}$ (specifically, $R_{max} = 7.5 \cdot 10^4$ mmHg s ml^{-1} and $R_{min} = 2.2 \cdot 10^{-2}$ mmHg s ml^{-1});
3. *Follow-up*: we have the same scenario as in Post-PVR, where, however, the LPM parameters are different to account for the evolution of the patients' conditions (see Section 3.3.1).

Notice that the calibration of the LPM and 1-DoF valve model for all scenarios is carried out by using patient-specific data (see Section 3.3).

3.2 Geometries reconstruction

Pre-implantation CT scans are used to obtain patient-specific 3D pulmonary artery geometries for both P1 and P2. The patients' CT scans were provided by the Department of Cardiac Surgery of hospital ASST Grande Ospedale Metropolitano Niguarda, Milan, Italy. Ethical Review Board approval and informed consent from all patients were obtained. The segmentation process is carried out using VMTK [51, 52]. The reconstructed geometries include multiple outlets and we use Paraview [53] and VMTK to remove secondary branches. The final geometries are composed of the pulmonary trunk and two outflow regions which correspond to the two branches originating from the first bifurcation of the pulmonary artery (see Fig. 3, left).

The post-implantation cases, Post-PVR and Follow-up, are characterised by the same geometry, obtained from Pre-PVR geometries and virtually inserting the stent graft. Notice that the pulmonary trunk geometry is different from the Pre-PVR scenario due to the stent presence. The stent is modelled as a cylinder with the nominal length (20 mm) and diameter (29 mm) of the *No-React® BioPulmonic™* valve. This cylinder is positioned and oriented in accordance with the patient-specific position of the commissures reconstructed from post-implantation CT scans (Fig. 3, right).

As for the pulmonary valve, the resolution of the CT scans does not allow the reconstruction of the leaflets. Thus, a template valve model by Zygote [54] is adapted to the stent geometry to obtain the valve closed configuration. Afterwards, the open configuration is derived from the closed one by pure geometric deformation, opening the leaflets

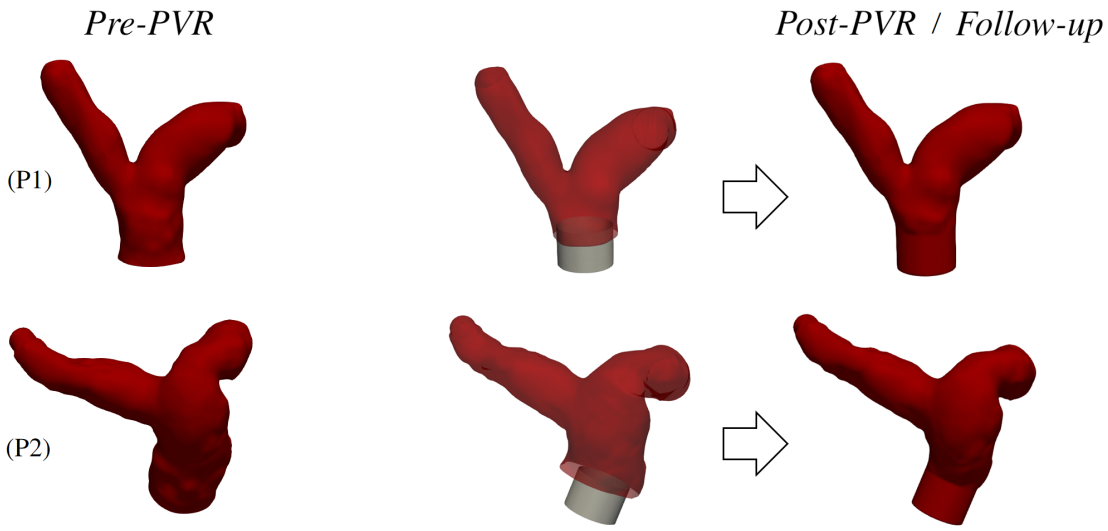

Figure 3: Reconstructed geometries used to build the three scenarios of both P1 and P2. Left: Pre-PVR as from image segmentation; Right: Virtual insertion of the PV stent to create the Post-PVR/Follow-up scenarios.

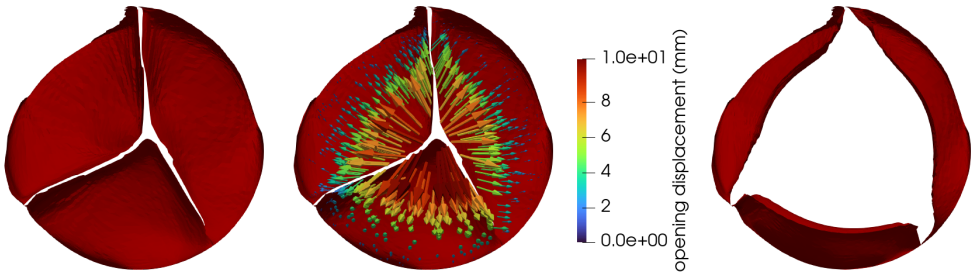

Figure 4: The closed configuration of the pulmonary valve (left), the displacement imposed to the leaflets surface to approximate the physiological behaviour of the valve in the open configuration (centre) and the open configuration (right).

compatibly with the surrounding stent to have a physiological orifice area (see Fig. 4). The prescribed deformation is then used in the rFSI model (5) as the variable $\mathbf{g}$.

The 3D fluid mesh generation is carried out in the same way for the Pre-PVR, Post-PVR and Follow-up scenarios. Specifically, we use a non uniform mesh characterised by a cell diameter $h = 1.1$ mm in the pulmonary trunk and $h = 4.3$ mm at the outlets (Fig. 5). This allowed us to have higher accuracy in the region where higher velocities and wall shear stresses are expected, and to properly capture the leaflets dynamics by the RIIS method.

The meshes used in this work are obtained after a mesh-independence study in the Pre-PVR scenarios where we checked that the Wall Shear Stress (WSS) differs by at most 2% when the mesh was refined by a 10% factor.

3.3 Calibration procedure

In the following section we detail the calibration procedure both for the LPM and the 1-DoF valve model. Specifically, the LPM is calibrated utilizing P1's patient-specific data we have at our disposal to obtain suitable boundary conditions (Section 3.3.1), while the 1-DoF model is calibrated employing literature data to reproduce a physiological dynamics of the valve (Section 3.3.2).

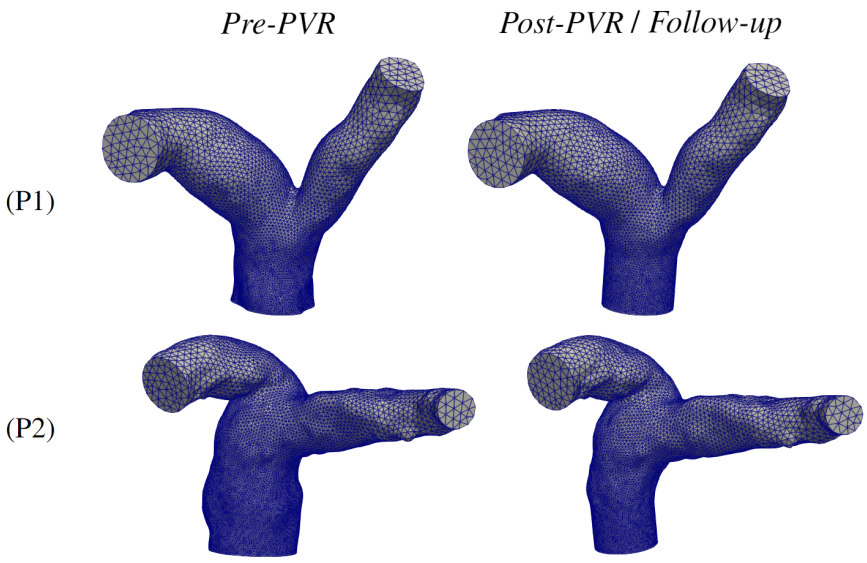

Figure 5: The meshes of P1 and P2 used in the three scenarios considered

	6 months after PVR	**9 years after PVR**
ESV (ml)	105	58
EDV (ml)	165	110
EF%	35	47

Table 1: Clinical measurements of patient P1 for the calibration of the LPMs.

3.3.1 Lumped Parameters Models calibration

The LPMs calibration of all three scenarios relies on the use of P1's clinical data, see Table 1. Specifically, we create three different sets of calibrated LPM parameters, one for each scenario, and we use:

- the End-Systolic Volume (ESV), i.e. the residual volume in the ventricle after the ejection of blood in the systolic phase;
- the End-Diastolic Volume (EDV), i.e. the volume in the ventricle at the end of diastole;
- the Ejection Fraction (EF), calculated as $\frac{EDV-ESV}{EDV}$.

Notice that the data measured 9 years after the PVR lie in physiological ranges found in the literature [55].

In the process of calibration, the LPM parameters are iteratively changed until the simulated EF is characterised by a small difference with respect to the corresponding measured value. For the calibration of the Post-PVR and Follow-up LPMs, we use the data at 6 months and 9 years after the PVR, respectively (Table 1). For the Pre-PVR scenario, there was no available data which described the patient's condition before the surgery; thus, we assume that the patient's clinical data before the surgery and 6 months after are comparable. This assumption is supported by [56], where EF values are shown to be very similar between the pre-implantation condition and 6 months after the surgery. Therefore, we use the Post-PVR clinical data also in the calibration of the Pre-PVR scenario; nevertheless, the two models will be distinguished by the absence and presence of the pulmonary valve.

Specifically, we assign the EDV of the right ventricle V_{RV} from P1's data and we calibrate the following parameters to match EF [25, 49]:

- The elastances of the right heart: E_a, E_b;
- The RLC circuit describing the pulmonary arterial circulation, composed by the resistance R_{art}, the capacitance C_{art} and the inductance I_{art};
- The non-ideal diode representing the pulmonary valve, modelled by two resistances and an inductance: R_{max}, R_{min}, I_v.

We also fix the right atrium EDV V_{RA} to the physiological value of 45 ml as reported in [57].

	Pre-PVR	**Post-PVR**	**Follow-up**
Used data (see Table 1)	6 months after PVR	6 months after PVR	9 years after PVR
Right ventricle			
E_a (mmHg ml^{-1})	0.07	0.10	0.24
E_b (mmHg ml^{-1})	0.09	0.08	0.08
Pulmonary arterial circulation			
R_{art} (mmHg s ml^{-1})	0.05	0.05	0.07
C_{art} (ml mmHg^{-1})	7.0	7.0	8.0
I_{art}(mmHg s^2 ml^{-1})	5e-3	5e-3	5e-3
Pulmonary valve			
R_{max} (mmHg s ml^{-1})	2.2e-2	7.5e4	7.5e4
R_{min} (mmHg s ml^{-1})	2.2e-2	2.2e-2	2.2e-2
V_{RA} (ml)	45	45	45
V_{RV} (ml)	165	165	110
EF%	35.1	38.8	52.9

Table 2: Calibrated parameters of the LPM, the initial volumes used for right ventricle V_{RV} and right atrium V_{RA}, and the EF value found by the numerical simulations of the circulation with the calibrated parameters for each scenario.

Parameters	**Values in Post-PVR/Follow-up scenarios**
β (s^{-1})	0.28
γ (s^{-2})	0.13
χ (m^{-1})	0.24
ρ_Γ (kg m^{-2})	106
α (-)	0.075

Table 3: Calibrated parameters for the reduced structural valve model in the Post-PVR and Follow-up scenarios.

The calibrated parameters in Table 2 allow to obtain EF values (also reported in Table 2) very close to P1's measures in Table 1: in the Pre-PVR scenario they differ by 0.3%, in the Post-PVR scenario by 10%, and in the Follow-up scenario by 12.5%.

3.3.2 Valve model calibration

In the Post-PVR and Follow-up scenarios, the 1-DoF model parameters are suitably set to achieve opening and closing times of the leaflets in accordance with the literature [58, 59]. The valve model calibration implies the tuning of 5 parameters:

- the *damping coefficient* (β in Eq. (3)) associated with the leaflets velocity;
- the *stiffness coefficient* (γ in (3)), associated with the elastic forces;
- the *added curvature* (χ in (3)) parameter;
- the *surface density* (ρ_Γ in (3)), associated to the inertial properties of the leaflets;
- the coefficient α introduced in the resistive penalty term in Eq. (1).

The calibration is performed by running various 3D rFSI simulations both for the Post-PVR and Follow-up scenarios using P1's computational domain until the opening and closing times of the leaflets were sufficiently close to the ones reported in the literature. The calibrated values are reported in Table 3.

With these calibrated parameters we obtain a valve dynamics close to the analysed literature [58, 59]; we report in Table 4 the values obtained from the simulation, regarding the duration of opening and closing times (namely the transitions of the opening coefficient c from 0 to 1 and from 1 to 0), and the open-state duration (the period when c stays equal to 1) for P1. Notice that we make the assumption that the valve properties remain unaltered from the Post-PVR to the Follow-up, so the same calibrated parameters are used in both cases.

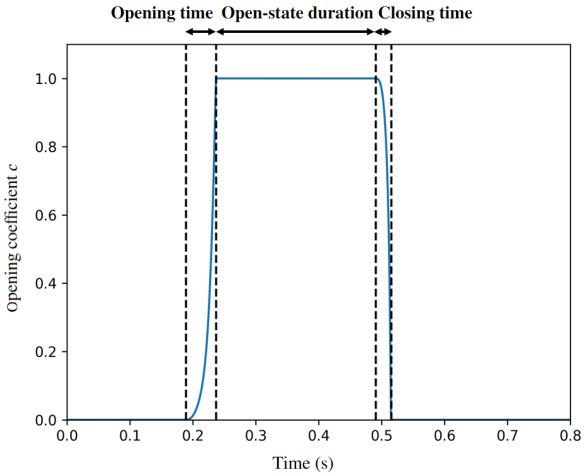

	Opening time (ms)	**Open-state duration** (ms)	**Closing time** (ms)
Post-PVR (P1)	104	336	47
Follow-up (P1)	47	254	23

Table 4: Computed timings of opening and closing of the simulated pulmonary valve dynamics both for the *Post* and *Follow-up* scenarios for P1.

4 Results and discussion

In this section we present and discuss the results of the 3D rFSI simulations in the three scenarios previously described (Section 3.1).

4.1 Settings of the numerical experiments

The parameters of the rFSI model and LPM model are set according to the result of the calibration procedures reported in Section 3.3. We make the assumption that, since the model describes the same valve implanted in both patients, the calibrated valve parameters found for P1 can be applied also to the numerical simulations of P2. This approach yields acceptable values of valve opening and closure times also for P2: for example, the opening time is 66 ms and 46 ms in the Post-PVR and Follow-up scenarios, respectively.

Moreover, we set $\rho = 1.06 \cdot 10^3$ kg m^{-3}, $\mu = 3.5 \cdot 10^{-3}$ Pa s, $R = 10^4$ kg m $^{-1}$ s^{-1} and $\varepsilon = 1.8$ mm, and the coefficient α in (5c) is set to 0.075 in order to reproduce more physiological results and enhance stability. Indeed, by using $\alpha = 1$ (which would guarantee a fully consistent no-slip condition) we were not able to recover stable results. Notice that our choice is intermediate between the fully consistent and the quasi-static ($\alpha = 0$) conditions, thus formally violating the physical adherence of the blood to the valve. However, since the quasi-static assumption has been widely used in the literature [60], we believe that our choice is acceptable. Also, the value of ε is chosen in order to satisfy the condition $\varepsilon > 1.5\, h$, necessary for the correct resolution of $\delta^n_{\varepsilon,h}$ in the resistive model [39].

Regarding the time discretisation parameter, we set $\Delta t = 5 \cdot 10^{-4}$ s for both LPM and rFSI problems. This value is chosen after a convergence analysis showing that, by halving Δt, the quantities of interest do not change by more than 2%. This value of the time step also allows us to satisfy the stability conditions associated with the explicit coupling between the 3D fluid model and the 1-DoF structural valve model.

To obtain the boundary conditions (6) for the rFSI model, we simulate offline six cardiac cycles of the LPM model. Each cardiac cycle starts from the end of diastole and has a period $T = 0.8$ s. Only the last one is analysed and used to extract the pressure curves to be prescribed at the inlet and outlets of the 3D pulmonary artery geometry (Fig. 6, top); these conditions result in a pressure gradient across the valve displayed in Fig. 6, bottom. As for the solution of the rFSI model, we simulate two cardiac cycles; the results shown in the next sections are extracted from the second simulated cardiac cycle.

In Table 5, we provide an overview of the main settings used for the simulations in the three scenarios.

4.2 Velocity and pressure analysis

We start the discussion of the results by analysing systolic blood flow velocities for the Pre-PVR and Follow-up scenarios; specifically, we observe the instant characterised by the maximum blood velocity. In the velocity plots of Fig. 7, left, we notice that the blood velocity is higher in the Follow-up scenario than in the Pre-PVR. In particular, after the valve implantation, the peak velocity in the pulmonary artery reaches 130 cm/s; this value is higher than

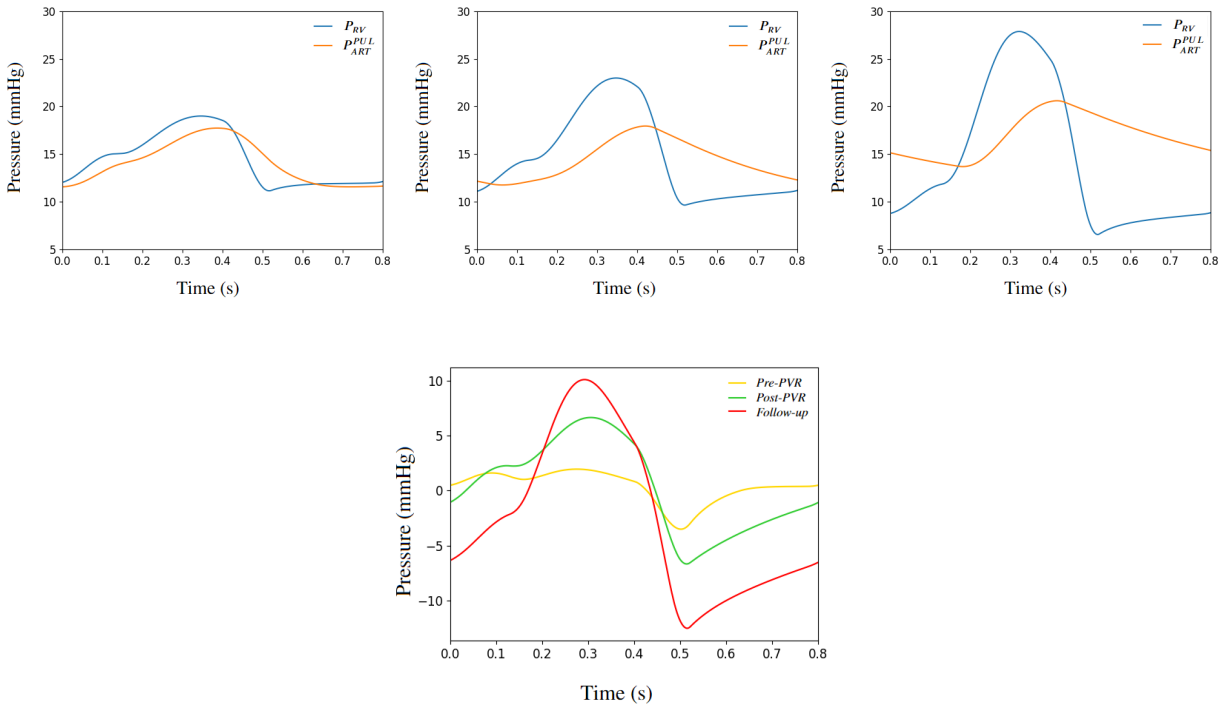

Figure 6: Top: Time-varying pressure boundary conditions computed by the 0D model and prescribed at the inlet (P^{RV}) and at the outlets (P_{ART}^{PUL}) of the 3D rFSI model for the three scenarios: Pre-PVR (left), Post-PVR (middle), Follow-up (right); Bottom: Corresponding pressure drops in the three simulated scenarios.

	Pre-PVR	**Post-PVR**	**Follow-up**
Geometry	absent valve	stent graft inserted, valve included	stent graft inserted, valve included
Data used for LPM calibration	6 months after PVR	6 months after PVR	9 years after PVR
RIIS term resistance	$R = 0$ kg m^{-1} s^{-1}	$R = 10^4$ kg m^{-1} s^{-1}	$R = 10^4$ kg m^{-1} s^{-1}
LPM valve resistances	$R_{max} = R_{min}$	$R_{max} >> R_{min}$	$R_{max} >> R_{min}$

Table 5: Synthesis of both P1's and P2's configuration of the three scenarios considered for the numerical simulations.

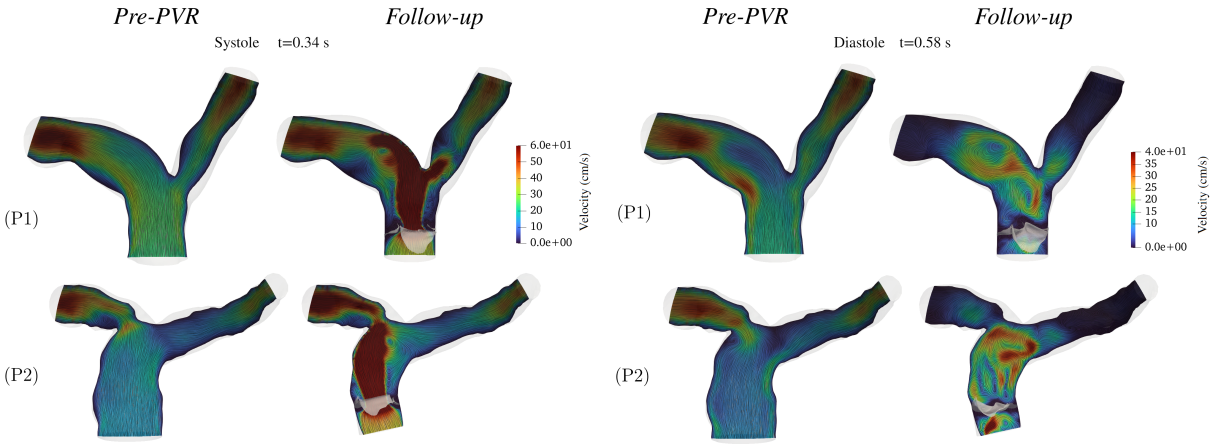

Figure 7: P1 and P2's velocity field in the Pre-PVR and Follow-up scenarios at t=0.34 s (systolic phase) and at t=0.58 s (diastolic phase).

	P1		**P2**	
	Pre-PVR	**Follow-up**	**Pre-PVR**	**Follow-up**
EV (ml)	63.9	33.3	54.3	35.3
RV (ml)	25.2	4.7	22.5	6.6
SV (ml)	38.7	28.6	31.8	28.7

Table 6: Values of EV, RV and SV computed in the 3D simulations of the the Pre-PVR and Follow-up scenarios for P1 and P2.

the physiological range of 60-100 cm/s [61], however, it can be found in patients with hypertrophy of the right heart, a condition which commonly affects patients that have suffered from Tetralogy of Fallot, as those analysed in the present work [62]. Moreover, we notice that the different points of impact of the fluid jet on the artery wall in P1's and P2's velocity plots (in Follow-up scenarios) put in evidence the effect of the pulmonary artery geometry and valve orientation on the velocity pattern.

As for the diastolic velocity field and flow rates (see Fig. 7, right), we observe that in the Follow-up scenario the closure of the valve prevents regurgitation, which occurs instead in the Pre-PVR scenario due to the valve absence. In Table 6 we report the computed right ventricle total Ejected Volume (EV), the Regurgitant Volume (RV) – defined as the volume that returns to the ventricle when the backflow is established – and the Stroke Volume SV = EV - RV. By computing the Regurgitant Fraction RF = (RV/EV) $\cdot$ 100, which is commonly used as a measure of pulmonary insufficiency, we obtain RF = 39.4% and RF = 41.4% in the Pre-PVR scenarios. From these results, we notice that about 40% of the blood ejected by the right ventricle during the cardiac cycle returns into the ventricle. The values found are coherent with the literature; in particular, a regurgitant fraction of 40% coincides with the condition of pulmonary valve severe insufficiency and constitutes an indication for pulmonary valve replacement [63]. On the contrary, in the Follow-up scenario, we notice a significant reduction in the RV, as expected after the valve implantation. Moreover, we observe that SV is only slightly reduced after the valve implantation.

In Fig. 8 we display the time evolution of flow rate through the valvular plane in time. We observe that the values of flow rate exiting the ventricle (positive values) reach a systolic peak of approximately 200 ml/s, coherent with the reference values for the pulmonary artery flow rate found in the literature [64].

In Fig. 9 we show the plots of the diastolic pressure for Pre-PVR, Post-PVR and Follow-up scenarios of the two patients. We notice that the pressure values are close to the physiological range, especially in the Follow-up scenario [65]. In this scenario, we can see how the closed valve sustains a significant pressure drop (see zoom in Fig. 9). This effect is less evident in the Post-PVR scenario, due to the lower pressure drop assigned through the boundary conditions. On the other end, in the Pre-PVR scenario the valve absence prevents the formation of a significant pressure gradient throughout the whole geometry.

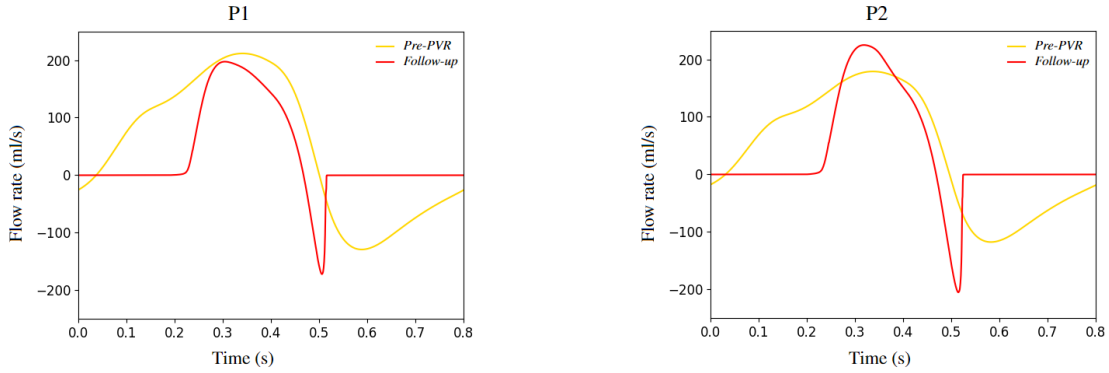

Figure 8: P1 and P2's flow rate through the valvular plane in the Pre-PVR and Follow-up simulated scenarios.

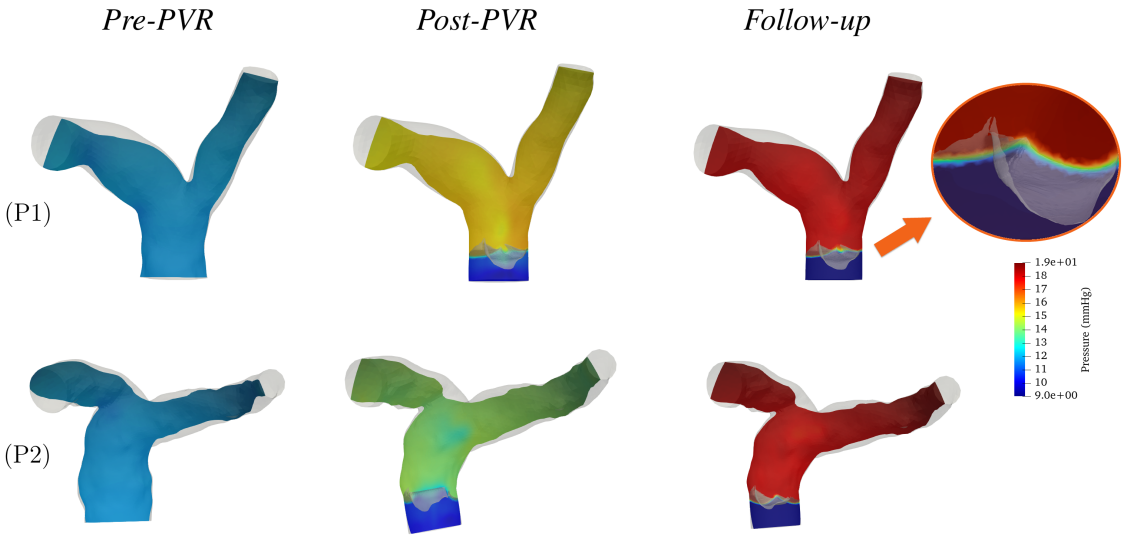

Figure 9: P1's and P2's pressure plots in the three simulated scenarios at the diastolic time t=0.58 s.

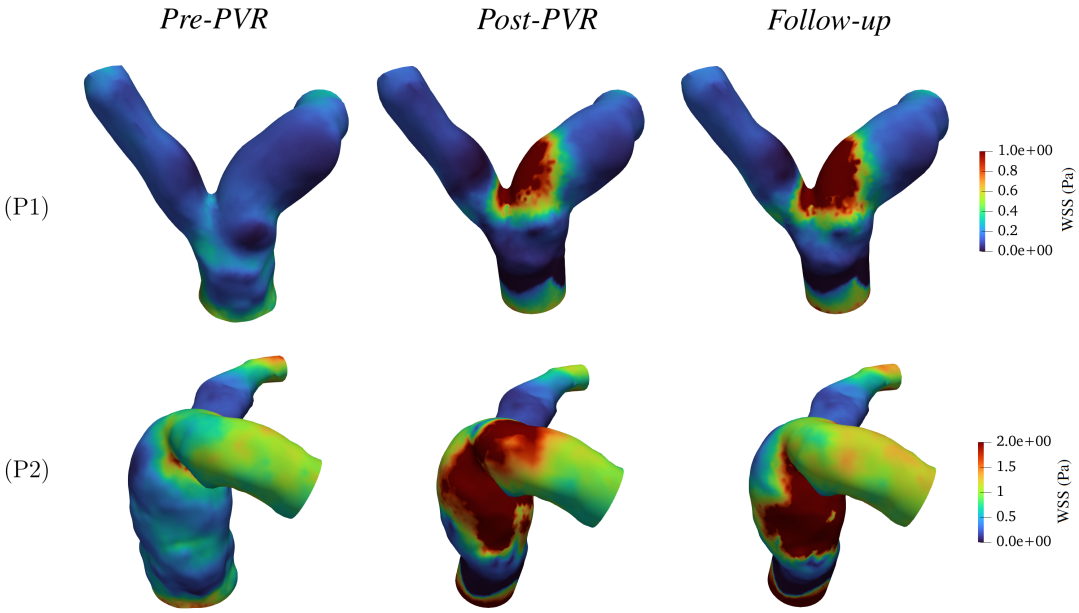

Figure 10: P1's and P2's Wall Shear Stress in the three simulated scenarios during the systolic phase (t=0.34 s).

4.3 Wall Shear Stress and turbulence analysis

From the velocity field we derive the Wall Shear Stress (WSS), namely the tangential force per unit area that is applied by the blood flowing on the surface of the pulmonary wall (Γ_{wall}), defined as [66]:

$$\text{WSS} = (\mu + \mu_{sgs}) \sqrt{\sum_{j=1}^{2} [(\nabla \mathbf{u} + \nabla \mathbf{u}^T)\, \mathbf{n} \cdot \tau_j]^2} \quad \text{on } \Gamma_{wall},$$

where $\tau_j, j = 1, 2$, are the tangential unit vectors. We report the result in Fig. 10, where we notice that the prosthetic valve significantly affects the distribution of the WSS along the artery wall. In particular, we notice that the WSS is higher in the Post-PVR and Follow-up scenarios, due to the higher velocity of the blood. Moreover, for these scenarios, high values of WSS identify the impingement region of the systolic jet, which is different between the patients due to the different geometries and valve orientations. This observation is consistent with those on the systolic velocity profiles reported in Section 4.2.

In Fig. 11 we display the turbulent viscosity ratio μ_{sgs}/μ, where μ_{sgs} is the turbulent viscosity of the LES σ-model; high values of μ_{sgs}/μ indicate a local regime of transition to turbulence [35, 36]. We notice that the viscosity ratio is much smaller in Pre-PVR than Post-PVR and Follow-up. In the latter two scenarios, during systole (Fig. 11, top) high values of μ_{sgs}/μ identify the vortices generated by the flow jet exiting the valve and its impact on the arterial wall. In diastole (Fig. 11, bottom), μ_{sgs}/μ puts in evidence the vortex breaking in the artery.

5 Concluding remarks and limitations

In this work we have studied the haemodynamics in the pulmonary artery in presence of pulmonary valve replacement. To do this we use a reduced FSI model based on the interaction between a 3D FSI and a 1-DoF valve model, here applied for the first time to a patient-specific scenario.

The major outcomes of the study are:

- If properly calibrated, as done in this work starting from patients' clinical measures, the proposed rFSI model proved to be reliable in reproducing haemodynamics quantities coherent with the patient's condition, allowing to verify the effects of the valve implantation on the pulmonary artery fluid dynamics;

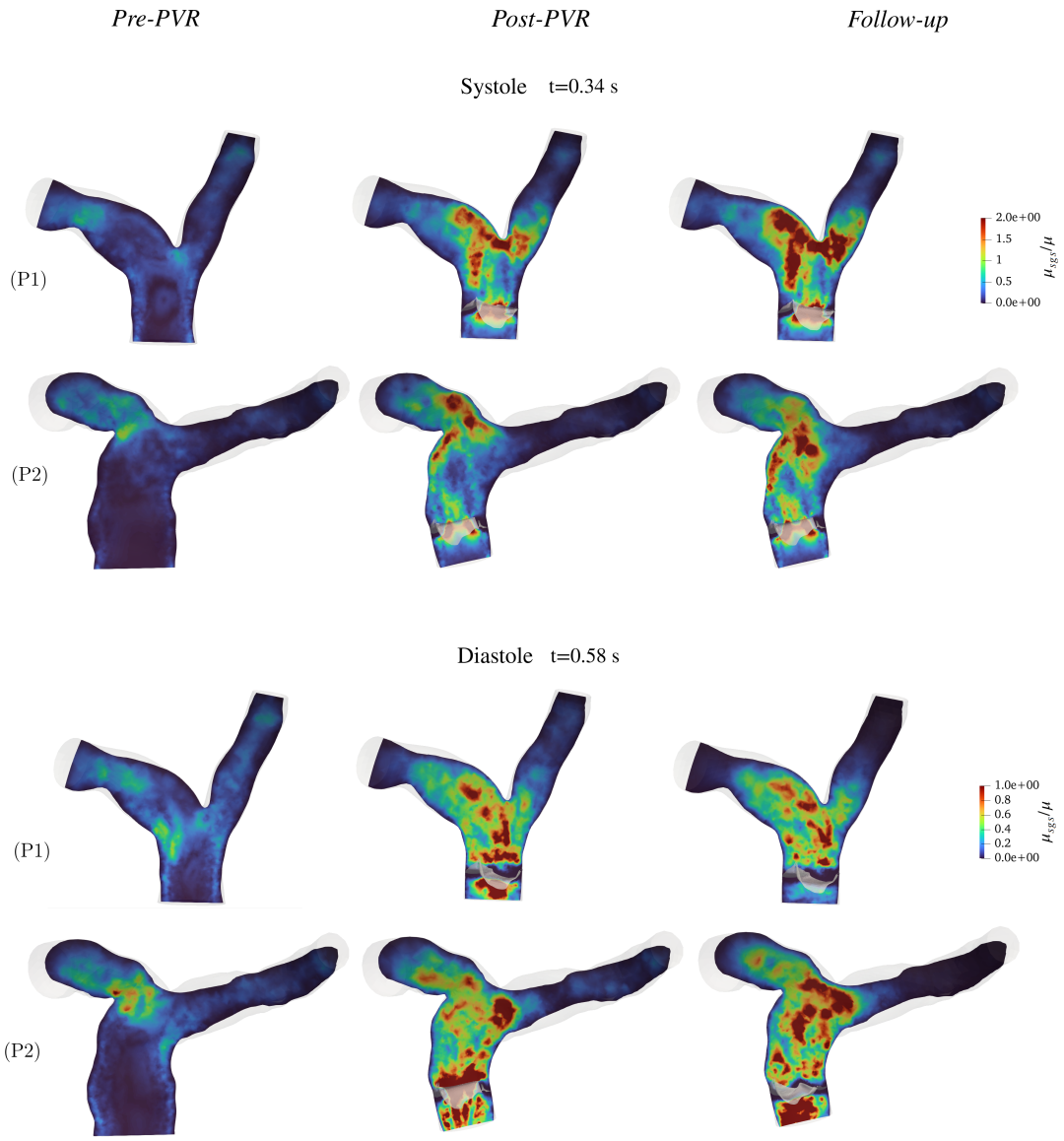

Figure 11: The ratio μ_{sgs}/μ for both P1 and P2 in the three scenarios analysed at time systolic time t=0.34 s and diastolic time t=0.58 s.

- This calibration proved to be robust with respect to the patient, indeed the calibration performed on P1's data was effective when applied also to P2;
- The rFSI model was able to well describe the diastolic pressure gradient across the pulmonary valve, obtaining values in accordance with PVR patients, slightly larger for Follow-up than Post-PVR scenario;
- As expected, the Post-PVR and Follow-up scenarios were characterised by larger values of velocity field, WSS, and turbulence, yet in a range in accordance with Tetralogy of Fallot patients.

We highlight some of the limitations encountered during the study:

- For P2, geometrical data were provided, but we lacked clinical haemodynamics measures. The validation against measures of other patients should be performed in future studies in order to further assess the robustness of our calibration;
- Due to the lack of measures regarding the patients' condition before the implantation, during the LPM calibration process we assumed that they could be well approximated by the same data used for Post-PVR scenario. Although acceptable, this limitation should be overcome in future studies by using pre-operative measures;
- The computed Follow-up flow rate across the valve showed to be characterised by a non-negligible level of regurgitation. Although the latter is in accordance with the patients' conditions, for future studies we need to better assess the rFSI model to reduce such effect.

Acknowledgments

IF has received support from ICSC–Centro Nazionale di Ricerca in High Performance Computing, Big Data, and Quantum Computing funded by European Union–NextGenerationEU, and from grant No. 740132, iHEART - An Integrated Heart Model for the simulation of the cardiac function, P.I. Prof. A. Quarteroni, funded by the European Research Council (ERC) under the European Union's Horizon 2020 research and innovation program. The present research is part of the activities of the project Dipartimento di Eccellenza 2023-2027, Dipartimento di Matematica, Politecnico di Milano. IF and CV are members of the INdAM group GNCS "Gruppo Nazionale per il Calcolo Scientifico" (National Group for Scientific Computing). CV has been partially supported by the Italian Ministry of University and Research (MIUR) within the PRIN (Research projects of relevant national interest) MIUR PRIN22-PNRR n. P20223KSS2 "Machine learning for fluid-structure interaction in cardiovascular problems: efficient solutions, model reduction, inverse problems", and by the Italian Ministry of Health within the PNC PROGETTO HUB - DIAGNOSTICA AVANZATA (HLS-DA) "INNOVA", PNC-E3-2022-23683266.

References

[1] A. G. Kidane, G. Burriesci, P. Cornejo, A. Dooley, S. Sarkar, P. Bonhoeffer, M. Edirisinghe, and A. M. Seifalian, "Current developments and future prospects for heart valve replacement therapy," *Journal of Biomedical Materials Research Part B: Applied Biomaterials: An Official Journal of The Society for Biomaterials, The Japanese Society for Biomaterials, and The Australian Society for Biomaterials and the Korean Society for Biomaterials*, vol. 88, no. 1, pp. 290–303, 2009.

[2] E. S. Fioretta, P. E. Dijkman, M. Y. Emmert, and S. P. Hoerstrup, "The future of heart valve replacement: recent developments and translational challenges for heart valve tissue engineering," *Journal of tissue engineering and regenerative medicine*, vol. 12, no. 1, pp. e323–e335, 2018.

[3] M. G. Nestola, P. Zulian, L. Gaedke-Merzhäuser, and R. Krause, "Fully coupled dynamic simulations of bioprosthetic aortic valves based on an embedded strategy for fluid–structure interaction with contact," *EP Europace*, vol. 23, no. Supplement_1, pp. i96–i104, 2021.

[4] A. B. Goldstone, P. Chiu, M. Baiocchi, B. Lingala, W. L. Patrick, M. P. Fischbein, and Y. J. Woo, "Mechanical or biologic prostheses for aortic-valve and mitral-valve replacement," *New England Journal of Medicine*, vol. 377, no. 19, pp. 1847–1857, 2017.

[5] S. J. Head, M. Çelik, and A. P. Kappetein, "Mechanical versus bioprosthetic aortic valve replacement," *European heart journal*, vol. 38, no. 28, pp. 2183–2191, 2017.

[6] S. Morganti, M. Conti, M. Aiello, A. Valentini, A. Mazzola, A. Reali, and F. Auricchio, "Simulation of transcatheter aortic valve implantation through patient-specific finite element analysis: Two clinical cases," *Journal of Biomechanics*, vol. 47, no. 11, pp. 2547–2555, 2014.

[7] A. M. Gillinov, E. H. Blackstone, E. R. Nowicki, W. Slisatkorn, G. Al-Dossari, D. R. Johnston, K. M. George, P. L. Houghtaling, B. Griffin, J. F. Sabik III, *et al.*, "Valve repair versus valve replacement for degenerative mitral valve disease," *The Journal of thoracic and cardiovascular surgery*, vol. 135, no. 4, pp. 885–893, 2008.

[8] J. Diaz-Frias and M. Guillaume, "Tetralogy of fallot," in *StatPearls [Internet]*, StatPearls Publishing, 2022.

[9] C. Apitz, G. D. Webb, and A. N. Redington, "Tetralogy of fallot," *The Lancet*, vol. 374, no. 9699, pp. 1462–1471, 2009.

[10] J. Forman, R. Beech, L. Slugantz, and A. Donnellan, "A review of tetralogy of Fallot and postoperative management," *Critical Care Nursing Clinics of North America*, vol. 31, no. 3, pp. 315–328, 2019.

[11] A. M. Sharkey and A. Sharma, "Tetralogy of Fallot: anatomic variants and their impact on surgical management," in *Seminars in cardiothoracic and vascular anesthesia*, vol. 16, pp. 88–96, SAGE Publications Sage CA: Los Angeles, CA, 2012.

[12] E. by the Association for European Paediatric Cardiology (AEPC), A. F. Members, H. Baumgartner, P. Bonhoeffer, N. M. De Groot, F. de Haan, J. E. Deanfield, N. Galie, M. A. Gatzoulis, C. Gohlke-Baerwolf, *et al.*, "Esc guidelines for the management of grown-up congenital heart disease (new version 2010) the task force on the management of grown-up congenital heart disease of the european society of cardiology (esc)," *European heart journal*, vol. 31, no. 23, pp. 2915–2957, 2010.

[13] P. Artemiou, I. Schusterova, A. Tohatyova, J. Cocherova, P. Krcho, and F. Sabol, "Follow-up after the ross procedure, how significant it is, case reports of three patients," *Journal of Cardiothoracic Surgery*, vol. 10, pp. 1–4, 2015.

[14] B. Ghitti, E. F. Toro, and L. O. Müller, "Nonlinear lumped-parameter models for blood flow simulations in networks of vessels," *ESAIM: Mathematical Modelling and Numerical Analysis*, vol. 56, no. 5, pp. 1579–1627, 2022.

[15] A. Quarteroni, A. Veneziani, and C. Vergara, "Geometric multiscale modeling of the cardiovascular system, between theory and practice," *Computer Methods in Applied Mechanics and Engineering*, vol. 302, pp. 193–252, 2016.

[16] H. J. Kim, I. E. Vignon-Clementel, C. A. Figueroa, J. F. LaDisa, K. E. Jansen, J. A. Feinstein, and C. A. Taylor, "On coupling a lumped parameter heart model and a three-dimensional finite element aorta model," *Annals of biomedical engineering*, vol. 37, pp. 2153–2169, 2009.

[17] S. Shimizu, D. Une, T. Kawada, Y. Hayama, A. Kamiya, T. Shishido, and M. Sugimachi, "Lumped parameter model for hemodynamic simulation of congenital heart diseases," *The journal of physiological sciences*, vol. 68, pp. 103–111, 2018.

[18] P. R. Trenhago, L. G. Fernandes, L. O. Müller, P. J. Blanco, and R. A. Feijóo, "An integrated mathematical model of the cardiovascular and respiratory systems," *International journal for numerical methods in biomedical engineering*, vol. 32, no. 1, p. e02736, 2016.

[19] P. J. Kilner, R. Balossino, G. Dubini, S. V. Babu-Narayan, A. M. Taylor, G. Pennati, and F. Migliavacca, "Pulmonary regurgitation: the effects of varying pulmonary artery compliance, and of increased resistance proximal or distal to the compliance," *International journal of cardiology*, vol. 133, no. 2, pp. 157–166, 2009.

[20] B. T. Tang, T. A. Fonte, F. P. Chan, P. S. Tsao, J. A. Feinstein, and C. A. Taylor, "Three-dimensional hemodynamics in the human pulmonary arteries under resting and exercise conditions," *Annals of biomedical engineering*, vol. 39, pp. 347–358, 2011.

[21] B. T. Tang, S. S. Pickard, F. P. Chan, P. S. Tsao, C. A. Taylor, and J. A. Feinstein, "Wall shear stress is decreased in the pulmonary arteries of patients with pulmonary arterial hypertension: an image-based, computational fluid dynamics study," *Pulmonary circulation*, vol. 2, no. 4, pp. 470–476, 2012.

[22] M. Boumpouli, E. L. Sauvage, C. Capelli, S. Schievano, and A. Kazakidi, "Characterization of flow dynamics in the pulmonary bifurcation of patients with repaired tetralogy of fallot: A computational approach," *Frontiers in Cardiovascular Medicine*, vol. 8, p. 703717, 2021.

[23] S. Aslan, M. Guillot, N. Ross-Ascuitto, and R. Ascuitto, "Hemodynamics in a bidirectional glenn shunt supplemented with a modified blalock-taussig shunt: Computational fluid dynamics assessment," *Progress in Pediatric Cardiology*, vol. 60, p. 101256, 2021.

[24] I. E. Vignon-Clementel, A. L. Marsden, and J. A. Feinstein, "A primer on computational simulation in congenital heart disease for the clinician," *Progress in Pediatric Cardiology*, vol. 30, no. 1-2, pp. 3–13, 2010.

[25] F. Marcinno', A. Zingaro, I. Fumagalli, L. Dede', and C. Vergara, "A computational study of blood flow dynamics in the pulmonary arteries," *Vietnam Journal of Mathematics*, vol. 51, no. 1, pp. 127–149, 2023.

[26] A. Baretta, C. Corsini, W. Yang, I. E. Vignon-Clementel, A. L. Marsden, J. A. Feinstein, T.-Y. Hsia, G. Dubini, F. Migliavacca, G. Pennati, *et al.*, "Virtual surgeries in patients with congenital heart disease: a multi-scale modelling test case," *Philosophical Transactions of the Royal Society A: Mathematical, Physical and Engineering Sciences*, vol. 369, no. 1954, pp. 4316–4330, 2011.

[27] C. Corsini, D. Cosentino, G. Pennati, G. Dubini, T.-Y. Hsia, and F. Migliavacca, "Multiscale models of the hybrid palliation for hypoplastic left heart syndrome," *Journal of biomechanics*, vol. 44, no. 4, pp. 767–770, 2011.

[28] J. Liu, W. Yang, I. S. Lan, and A. L. Marsden, "Fluid-structure interaction modeling of blood flow in the pulmonary arteries using the unified continuum and variational multiscale formulation," *Mechanics research communications*, vol. 107, p. 103556, 2020.

[29] F. Kong, V. Kheyfets, E. Finol, and X.-C. Cai, "Simulation of unsteady blood flows in a patient-specific compliant pulmonary artery with a highly parallel monolithically coupled fluid-structure interaction algorithm," *International journal for numerical methods in biomedical engineering*, vol. 35, no. 7, p. e3208, 2019.

[30] W. Yang, M. Dong, M. Rabinovitch, F. P. Chan, A. L. Marsden, and J. A. Feinstein, "Evolution of hemodynamic forces in the pulmonary tree with progressively worsening pulmonary arterial hypertension in pediatric patients," *Biomechanics and modeling in mechanobiology*, vol. 18, no. 3, pp. 779–796, 2019.

[31] B. A. Zambrano, N. McLean, X. Zhao, J.-L. Tan, L. Zhong, C. A. Figueroa, L. C. Lee, and S. Baek, "Patient-specific computational analysis of hemodynamics and wall mechanics and their interactions in pulmonary arterial hypertension," *Frontiers in bioengineering and biotechnology*, vol. 8, p. 611149, 2021.

[32] F. Capuano, Y.-H. Loke, and E. Balaras, "Blood flow dynamics at the pulmonary artery bifurcation," *Fluids*, vol. 4, no. 4, p. 190, 2019.

[33] F. M. Montevecchi and A. Redaelli, *Biomeccanica: analisi multiscala di tessuti biologici*. Pàtron, 2012.

[34] N. Bessonov, A. Sequeira, S. Simakov, Y. Vassilevskii, and V. Volpert, "Methods of blood flow modelling," *Mathematical modelling of natural phenomena*, vol. 11, no. 1, pp. 1–25, 2016.

[35] F. Nicoud, H. B. Toda, O. Cabrit, S. Bose, and J. Lee, "Using singular values to build a subgrid-scale model for large eddy simulations," *Physics of fluids*, vol. 23, no. 8, 2011.

[36] R. M. Lancellotti, C. Vergara, L. Valdettaro, S. Bose, and A. Quarteroni, "Large eddy simulations for blood dynamics in realistic stenotic carotids," *International journal for numerical methods in biomedical engineering*, vol. 33, no. 11, p. e2868, 2017.

[37] L. Bennati, C. Vergara, V. Giambruno, I. Fumagalli, A. F. Corno, A. Quarteroni, G. Puppini, and G. B. Luciani, "An image-based computational fluid dynamics study of mitral regurgitation in presence of prolapse," *Cardiovascular Engineering and Technology*, pp. 1–19, 2023.

[38] M. A. Fernández, J.-F. Gerbeau, and V. Martin, "Numerical simulation of blood flows through a porous interface," *ESAIM: Mathematical Modelling and Numerical Analysis*, vol. 42, no. 6, pp. 961–990, 2008.

[39] M. Fedele, E. Faggiano, L. Dedè, and A. Quarteroni, "A patient-specific aortic valve model based on moving resistive immersed implicit surfaces," *Biomechanics and modeling in mechanobiology*, vol. 16, pp. 1779–1803, 2017.

[40] I. Fumagalli, M. Fedele, C. Vergara, S. Ippolito, F. Nicolò, C. Antona, R. Scrofani, A. Quarteroni, *et al.*, "An image-based computational hemodynamics study of the systolic anterior motion of the mitral valve," *Computers in Biology and Medicine*, vol. 123, p. 103922, 2020.

[41] I. Fumagalli, "A reduced 3d-0d fsi model of the aortic valve including leaflets curvature," *arXiv preprint arXiv:2106.00571*, 2021.

[42] A. Quarteroni, R. Sacco, and F. Saleri, *Numerical mathematics*, vol. 37. Springer Science & Business Media, 2010.

[43] Y. Bazilevs, V. Calo, J. Cottrell, T. Hughes, A. Reali, and G. Scovazzi, "Variational multiscale residual-based turbulence modeling for large eddy simulation of incompressible flows," *Computer methods in applied mechanics and engineering*, vol. 197, no. 1-4, pp. 173–201, 2007.

[44] D. Forti and L. Dedè, "Semi-implicit bdf time discretization of the navier–stokes equations with vms-les modeling in a high performance computing framework," *Computers & Fluids*, vol. 117, pp. 168–182, 2015.

[45] P. C. Africa, I. Fumagalli, M. Bucelli, A. Zingaro, M. Fedele, L. Dede', and A. Quarteroni, "lifex-cfd: an open-source computational fluid dynamics solver for cardiovascular applications," *Computer Physics Communication*, 2023. Accepted. Preprint: arXiv 2023;2304.12032.

[46] P. C. Africa, "lifex: A flexible, high performance library for the numerical solution of complex finite element problems," *SoftwareX*, vol. 20, 2022.

[47] "Official website:." `https://lifex.gitlab.io/`. Binaries accessible at `https://zenodo.org/doi/10.5281/zenodo.6941115` (`life`$^{\text{x}}$), `https://zenodo.org/doi/10.5281/zenodo.7852088` (`life`$^{\text{x}}$-cfd).

[48] P. J. Blanco and R. A. Feijóo, "A 3d-1d-0d computational model for the entire cardiovascular system," *Mecánica Computacional*, vol. 29, no. 59, pp. 5887–5911, 2010.

[49] F. Regazzoni, M. Salvador, P. C. Africa, M. Fedele, L. Dedè, and A. Quarteroni, "A cardiac electromechanical model coupled with a lumped-parameter model for closed-loop blood circulation," *Journal of Computational Physics*, vol. 457, p. 111083, 2022.

[50] S. Ghiselli, C. Carro, N. Uricchio, G. Annoni, and S. M. Marianeschi, "Mid-to long-term follow-up of pulmonary valve replacement with biointegral injectable valve," *European Journal of Cardio-Thoracic Surgery*, vol. 59, no. 2, pp. 325–332, 2021.

[51] VMTK, Vascular, Modeling, and Toolkit. `http://www.vmtk.org/index.html`.

[52] M. Fedele and A. Quarteroni, "Polygonal surface processing and mesh generation tools for the numerical simulation of the cardiac function," *International Journal for Numerical Methods in Biomedical Engineering*, vol. 37, no. 4, p. e3435, 2021.

[53] Paraview. `https://www.paraview.org/`.

[54] Zygote. `http://www.zygote.com`.

[55] S. Wang, S. Wang, Q. Zhu, Y. Wang, G. Li, F. Kong, J. Yang, and C. Ma, "Reference values of right ventricular volumes and ejection fraction by three-dimensional echocardiography in adults: a systematic review and meta-analysis," *Frontiers in Cardiovascular Medicine*, vol. 8, p. 709863, 2021.

[56] T. Geva, K. Gauvreau, A. J. Powell, F. Cecchin, J. Rhodes, J. Geva, and P. del Nido, "Randomized trial of pulmonary valve replacement with and without right ventricular remodeling surgery," *Circulation*, vol. 122, no. 11_suppl_1, pp. S201–S208, 2010.

[57] R. M. Lang, L. P. Badano, V. Mor-Avi, J. Afilalo, A. Armstrong, L. Ernande, F. A. Flachskampf, E. Foster, S. A. Goldstein, T. Kuznetsova, *et al.*, "Recommendations for cardiac chamber quantification by echocardiography in adults: an update from the american society of echocardiography and the european association of cardiovascular imaging," *European Heart Journal-Cardiovascular Imaging*, vol. 16, no. 3, pp. 233–271, 2015.

[58] G. Tasca, R. Vismara, F. Trinca, B. Riva, A. Gamba, and E. Lobiati, "Opening/closing pattern of trifecta and freestyle valves versus native aortic valve: Are stentless valves more physiologic than a stented valve?," *Journal of Cardiac Surgery*, vol. 32, pp. 680–685, 11 2017.

[59] M. Handke, G. Heinrichs, F. Beyersdorf, M. Olschewski, C. Bode, and A. Geibel, "In vivo analysis of aortic valve dynamics by transesophageal 3-dimensional echocardiography with high temporal resolution," *The Journal of thoracic and cardiovascular surgery*, vol. 125, no. 6, pp. 1412–1419, 2003.

[60] A. This, H. G. Morales, O. Bonnefous, M. A. Fernández, and J.-F. Gerbeau, "A pipeline for image based intracardiac cfd modeling and application to the evaluation of the pisa method," *Computer Methods in Applied Mechanics and Engineering*, vol. 358, p. 112627, 2020.

[61] B. Bouhemad, F. Ferrari, K. Leleu, C. Arbelot, Q. Lu, and J.-J. Rouby, "Echocardiographic doppler estimation of pulmonary artery pressure in critically ill patients with severe hypoxemia," *The Journal of the American Society of Anesthesiologists*, vol. 108, no. 1, pp. 55–62, 2008.

[62] H. B. Grotenhuis, L. J. Kroft, S. G. van Elderen, J. J. Westenberg, J. Doornbos, M. G. Hazekamp, H. W. Vliegen, J. Ottenkamp, and A. de Roos, "Right ventricular hypertrophy and diastolic dysfunction in arterial switch patients without pulmonary artery stenosis," *Heart*, vol. 93, no. 12, pp. 1604–1608, 2007.

[63] A. Frigiola, V. Tsang, J. Nordmeyer, P. Lurz, C. van Doorn, A. M. Taylor, P. Bonhoeffer, and M. de Leval, "Current approaches to pulmonary regurgitation," *European Journal of Cardio-thoracic Surgery*, vol. 34, pp. 576–581, 9 2008.

[64] T. Wehrum, P. Hagenlocher, T. Lodemann, W. Vach, I. Dragonu, A. Hennemuth, C. von Zur Mühlen, J. Stuplich, B. T. T. Ngo, and A. Harloff, "Age dependence of pulmonary artery blood flow measured by 4d flow cardiovascular magnetic resonance: results of a population-based study," *Journal of Cardiovascular Magnetic Resonance*, vol. 18, pp. 1–9, 2016.

[65] G. Kovacs, A. Berghold, S. Scheidl, and H. Olschewski, "Pulmonary arterial pressure during rest and exercise in healthy subjects: a systematic review," *European Respiratory Journal*, vol. 34, no. 4, pp. 888–894, 2009.

[66] A. Quarteroni, A. Manzoni, and C. Vergara, "The cardiovascular system: Mathematical modelling, numerical algorithms and clinical applications," *Acta Numerica*, vol. 26, pp. 365–590, 5 2017.

MOX Technical Reports, last issues

Dipartimento di Matematica
Politecnico di Milano, Via Bonardi 9 - 20133 Milano (Italy)

108/2023 Arnone, E.; Negri, L.; Panzica, F.; Sangalli, L.M.
Analyzing data in complicated 3D domains: smoothing, semiparametric regression and functional principal component analysis

106/2023 Fontana, N.; Savaré, L.; Ieva, F.
Integrating state-sequence analysis to uncover dynamic drug-utilization patterns to profile heart failure patients

109/2023 Clementi, L.; Arnone, E.; Santambrogio, M.D.; Franceschetti, S.; Panzica, F.; Sangalli, L.M.
Anatomically compliant modes of variations: new tools for brain connectivity

105/2023 Cicci, L.; Fresca, S.; Guo, M.; Manzoni, A.; Zunino, P.
Uncertainty quantification for nonlinear solid mechanics using reduced order models with Gaussian process regression

103/2023 Dimola N.; Kuchta M.; Mardal K.A.; Zunino P.
Robust Preconditioning of Mixed-Dimensional PDEs on 3d-1d domains coupled with Lagrange Multipliers

104/2023 Possenti, L.; Gallo, A.; Vitullo, P.; Cicchetti, A.; Rancati, T.; Costantino, M.L.; Zunino, P.
A computational model of the tumor microenvironment applied to fractionated radiotherapy

101/2023 Formaggia, L.; Zunino, P.
Hybrid dimensional models for blood flow and mass transport

100/2023 Vitullo, P.; Cicci, L.; Possenti, L.; Coclite, A.; Costantino, M.L.; Zunino, P.
Sensitivity analysis of a multi-physics model for the vascular microenvironment

98/2023 Lespagnol, F.; Grandmont, C.; Zunino, P.; Fernandez, M.A.
A mixed-dimensional formulation for the simulation of slender structures immersed in an incompressible flow

96/2023 Bonetti, S.; Botti, M.; Antonietti, P.F.
Robust discontinuous Galerkin-based scheme for the fully-coupled non-linear thermo-hydro-mechanical problem